



Contrastive analysis of temperature and stress field distribution in cladding layer by the Gaussian and hollow-ring laser modes

Gangxian Zhu¹ · Guangqi Li¹ · Lifang Wang² · Shihong Shi¹

Received: 21 June 2022 / Accepted: 18 June 2023 / Published online: 17 July 2023
© The Author(s), under exclusive licence to Springer-Verlag London Ltd., part of Springer Nature 2023

Abstract

The Gaussian laser mode can be converted into a hollow-ring laser mode through beam conversion system, realizing the conversion of circular and solid spot into a hollow-ring spot, which changes the energy distribution form of the laser spot. In order to study the effects of the Gaussian and hollow-ring laser modes on temperature and stress fields in cladding layers, the numerical simulation and experimental investigation were performed. The results showed that molten pool experienced once temperature peak and generated sharp temperature change under the Gaussian laser, while the molten pool experienced twice temperature peaks and temperature changed relatively gentle when using hollow-ring laser. Comparing with the Gaussian laser, the maximum temperature gradient along the depth of cladding layer decreased by 72.3% from 1.79×10^6 to 4.95×10^5 °C/m, and the maximum residual stress decreased from 272 to 251 MPa under hollow-ring laser. Meanwhile, the simulation results were validated by experiments with the same process. Furthermore, the sample microstructure was studied from the experiment. The microstructure was finer and more uniform using hollow-ring laser. This paper can provide guidance and advantage for laser cladding and direct metal deposition based on the hollow-ring mode and expand the application of laser field.

Keywords Laser cladding · Hollow-ring laser · Residual stress · Numerical simulation · Defocusing amount

1 Introduction

Laser cladding is an advanced surface strengthening technology that uses a high-energy density laser as heat source to rapidly melt the metal powder and form a metallurgical combination with the substrate after solidification. Laser cladding has many advantages, such as little deformation of substrate, high hardness, well abrasion resistance, high corrosion resistance, and oxidation resistance [1], and has broad application prospects in fields of aerospace, automotive,

medical, nuclear, and shipping [2]. During laser cladding process, local heat input will inevitably lead to an uneven temperature field and a large temperature gradient. After cooling, it is easy to generate residual stress in cladding layers. High residual stress has an undesirable effect on the crack sensitivity, deformation of substrate, yield strength, ultimate strength, and fatigue strength, as well as the life expectancy of materials, which affects the mechanical properties of formed parts in turn [3]. Therefore, how to solve the residual stress problem has become a hot issue in the field of laser cladding. At present, numerical simulation combining experimental investigation is mostly used to study and predict the residual stress distribution of cladding layer under the Gaussian laser source [4].

Sun et al. built the 3D finite element model to simulate the temperature and stress field distribution in the process of laser cladding nicked-base alloys, and the results showed that a large temperature gradient was generated near the heat source, which easily caused high residual stress. And the cladding layer cracked along the vertical direction [5]. Wang performed numerical simulation and experimental research on the effects of process parameters

Gangxian Zhu and Guangqi Li have contributed equally to this work.

✉ Gangxian Zhu
gxzhu@suda.edu.cn

✉ Lifang Wang
lfiwang@suda.edu.cn

¹ School of Mechanical and Electrical Engineering, Soochow University, Suzhou, China

² Engineering Training Center, Soochow University, Suzhou, China

on residual stress during laser deposition forming, and the results showed that the residual stress on the top surface of the cladding layer decreased with scanning speed and preheating temperature increasing [6]. Heigel et al. adopted the thermal–mechanical coupling finite element method to study the stress evolution rule of TC4 titanium alloy during laser deposition, and the results showed that large temperature gradient caused high residual stress and plastic deformation [7]. Yan et al. explored the effect of process parameters on the deformation of cladding layer 316L stainless steel powder, and the results showed that laser power and powder feeding rate had a greater effect on the deformation of the cladding layer, and reducing the powder feeding rate and laser power could effectively reduce the temperature gradient distribution, which reduced residual stress and deformation of the cladding layer [8]. Krzyzanowski et al. studied the transient thermal and stress distributions with a numerical model during laser cladding, and they found that the crack susceptibility was reduced by the preheated base plate [9]. Wang et al. studied the influence of process parameters on thermal behavior during laser cladding of Ti-6Al-4 V metal powder by finite element method and concluded that the increasing laser power could increase the cooling rate and crack tendency of cladding layer [10]. Liu et al. discussed the effects of process parameters on thermal stress in a single-track cladding layer with wide-spot laser beam by numerical simulation, and the results showed that the laser power and scanning speed directly affected the solidification rate, temperature gradient, and cooling rate of the molten pool and stress increased with increasing of laser power and decreased with increasing of scanning speed [11].

Most of the above literatures focus on the Gaussian laser spot. The high energy is concentrated in the center of the spot, while the energy at the edge is low. Such energy distribution is easily to cause large temperature gradient in cladding. In addition, the adhering powder defects is often produced on both edges of the cladding layer with Gaussian laser spot in actual cladding process, which reduces the powder utilization rate. In order to solve the above defects caused by Gaussian laser spot, the research group invented a laser cladding nozzle device based on “hollow beam and internal powder feeding” cladding process [12]. The laser spot transformed from solid spot to hollow-ring spot by beam conversion system, and the energy distribution is more uniform, which can improve poor metallurgical bonding defect and enhance powder utilization rate [13]. Although much research on the temperature and stress field of Gaussian laser spot has been performed, the temperature and stress distribution with a hollow-ring laser spot has not been studied systematically. On account of different energy distributions, it is valuable to explore the temperature and stress fields with hollow-ring laser and expand the application of laser field.

2 Mechanism of hollow-ring laser cladding

2.1 Generation principle of hollow-ring laser spot

According to the coaxial nozzle device developed by our research group, the mechanism of hollow-ring spot is shown in Fig. 1. The powder feeding system consists of a powder feeder and a specially designed coaxial nozzle device, which makes the laser beam be split by a cone mirror and then focused by another ring mirror. Subsequently, the parallel beam is transferred into an internal hollow beam. By this method, the way of external-side powder feeding is transferred to inside-beam powder feeding, and the laser beam is guided to the worktable through an optical fiber and focused by an optical system with a 192 mm focal length to focus a hollow-ring laser spot. The powder tube is wrapped inside by the laser beam and drops vertically into the molten pool to avoid powder shunting, realizing the concentricity of the powder spot and the laser spot, the coaxiality of the powder flow and the laser beam, which greatly improves the utilization rate of metal powder.

2.2 Mathematical model of hollow-ring laser energy

Hollow-ring laser has a “Gaussian-like” energy distribution, and the energy density satisfies [14]

$$q_z(x, y) = \frac{\eta \cdot 2 \cdot P}{\pi(R_0^2 + 2R_0z \cot \varphi)} \exp\left(-\frac{2(\sqrt{x^2 + y^2} - (z \cot \varphi + \xi R_0))^2}{R_0^2}\right) \quad (1)$$

$$R_A = z \cot \varphi \quad (2)$$

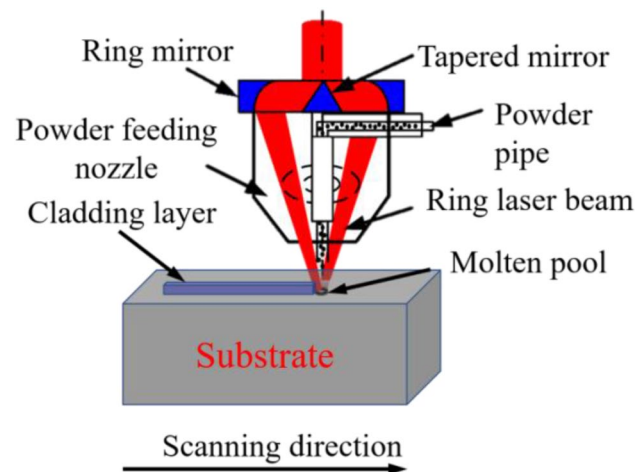


Fig. 1 Schematic diagram of hollow-ring spot generation

$$R_B = z \cot \varphi + R_0 \tag{3}$$

where

- P laser power, W
- η laser absorption efficiency
- R_0 radius at focal position, mm.
- z laser defocusing amount, the distance between the laser focus point and deposition point mm

The laser defocusing is defined as follows. The laser is focused when the laser focus point and deposition point are in coincidence, which is denoted by $z=0$ mm. Laser is in a negative defocusing situation when laser focus point is below deposition point, which is denoted by $z<0$ mm. Laser is in a positive defocusing situation when laser focus point is above deposition point, which is denoted by $z>0$ mm.

- φ the angle between the laser beam and the horizontal direction, °
- ξ energy peak position coefficient, $\xi \in [0 \sim 1]$
- R_A inner radius of ring spot, mm.
- R_B outer radius of ring spot, mm.

According to the formula, the energy distribution of the hollow-ring laser is related to the laser defocusing amount and the position of the energy peak. The energy values are obtained separately by taking different defocusing amounts and energy peak position coefficient. Considering the hollow-ring laser head structure used in the experiment, the energy peak is located in the middle of the ring region, so ξ is taken as 0.5 in this paper. In addition, the energy density satisfies the Gaussian energy distribution when $z=0$ according to formula 1.

So, the laser beam appears in the Gaussian mode when laser defocusing amount z is equal to 0, and the laser beam appears in hollow-ring laser mode when laser defocusing amount z is not equal to 0. Figure 2a shows the three-dimension energy and spot contour diagram of the Gaussian laser with $z=0$, and Fig. 2b shows the three-dimension energy and spot contour diagram of the hollow-ring laser with $z=-3$ mm.

As shown in Fig. 2b, the energy of the hollow-ring laser spot is concentrated in the ring region, and the central region presents low energy, which is contrary to the Gaussian energy distribution at Fig. 2a.

3 Finite element model theory

During laser cladding process, the melting and solidification of the molten pool are completed in an instant. The actual size of cladding layer is small, and the size of the molten pool is basically stable. To simplify the model calculation, the model is made in the following assumptions [15]:

- (1) The materials are all isotropic.
- (2) The ambient temperature is 25°C.
- (3) Both the cladding layer and the substrate are rectangular, ignoring subtle details such as rounded corners of the model.
- (4) The flow effect inside the molten pool is ignored.
- (5) Metal powder and substrate will not cause vaporization during cladding process.
- (6) The heat radiation effect is not considered separately and is equivalent coupled to convection heat transfer.

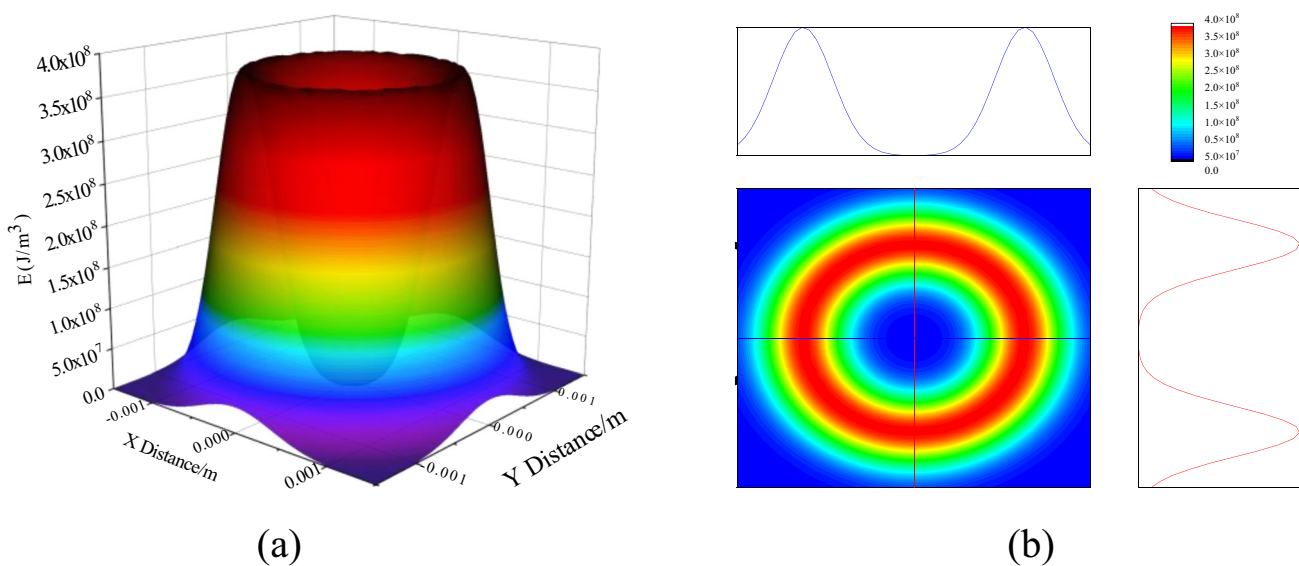


Fig. 2 Energy distribution and spot contour diagram

3.1 Thermal analysis

3.1.1 Governing equation

Laser cladding process is a typical transient heat transfer process. The transient heat source control equation satisfies the first law of thermodynamics and the Fourier heat equation [16]:

$$\rho c \frac{\partial T}{\partial t} = k \left(\frac{\partial^2 T}{\partial x^2} + \frac{\partial^2 T}{\partial y^2} + \frac{\partial^2 T}{\partial z^2} \right) + Q_{\text{laser}} \quad (4)$$

where ρ ($\text{kg} \cdot \text{m}^{-3}$) is the material density, k ($\text{W} \cdot \text{m}^{-1} \cdot \text{K}^{-1}$) and c ($\text{J} \cdot \text{kg}^{-1} \cdot \text{K}^{-1}$), respectively, represent the thermal conductivity and specific heat capacity of the material, and Q_{laser} ($\text{W} \cdot \text{m}^2$) represents the input laser energy.

3.1.2 Initial and boundary conditions

When the cladding process is not performed, the substrate has a uniform room temperature, which is the initial temperature.

$$T(x, y, z, t = 0) = T_0 \quad (5)$$

T_0 stands for room temperature, and the default value is 25 °C.

During laser cladding process, the heat conversion mainly includes the heat absorbed by the metal powder and the heat lost and radiated by the convective heat exchange between the workpiece and the surrounding environment. According to the law of conservation of energy, the boundary conditions are.

$$-k \frac{\partial T}{\partial n} = h(T - T_0) \quad (6)$$

In the formula, T and T_0 represent the boundary temperature and the room temperature, respectively, and h represents the comprehensive coefficient considering the effects of convection and radiation. The formula for calculating the comprehensive coefficient is as follows [17]:

$$h = 24.1 \times 10^{-4} \varepsilon T^{1.61} \quad (7)$$

where ε is the surface emissivity.

The top surface is set to.

$$-k \frac{\partial T}{\partial n} = Q_{\text{laser}} - h_1(T - T_0) - \sigma \varepsilon (T^4 - T_0^4) \quad (8)$$

where $h_1 = 100 \text{ W} \cdot (\text{m}^2 \cdot \text{K})^{-1}$ represents the convection coefficient between the molten pool and the surrounding environment; $\sigma = 5.67 \times 10^{-8} \text{ W} \cdot (\text{m}^2 \cdot \text{K}^4)^{-1}$ represents the Stefan–Boltzmann constant.

The boundary conditions at the bottom of the substrate are.

$$-k \frac{\partial T}{\partial n} = h_2(T - T_0) \quad (9)$$

where h_2 represents the convection coefficient between the substrate bottom and the worktable, $h_2 = 30 \text{ W} \cdot (\text{m}^2 \cdot \text{K})^{-1}$ [18].

The rest of surfaces are set to the following boundary conditions:

$$-k \frac{\partial T}{\partial n} = h_3(T - T_0) \quad (10)$$

where h_3 is the natural convection coefficient, $h_3 = 18 \text{ W} \cdot (\text{m}^2 \cdot \text{K})^{-1}$ [19].

3.2 Mechanical analysis

A thermal-elastic–plastic model is adopted to simulate the stress field. The total strain increment includes the following [20]:

$$\Delta \varepsilon = \Delta \varepsilon^e + \Delta \varepsilon^p + \Delta \varepsilon^T + \Delta \varepsilon^{\Delta V} + \Delta \varepsilon^{Trp} \quad (11)$$

where $\Delta \varepsilon^e$, $\Delta \varepsilon^p$, $\Delta \varepsilon^T$ and represent the elastic strain increment, plastic strain increment, and thermal strain increment respectively, $\Delta \varepsilon^{\Delta V}$ represents volumetric strain increment, and $\Delta \varepsilon^{Trp}$ represents strain increment caused by phase change.

In stress field analysis, the initial boundary conditions are

$$\sigma(x, y, z, 0) = 0, \varepsilon(x, y, z, 0) = 0 \quad (12)$$

Two sides of the substrate are subject to displacement constraints, which is in line with the fixture fixing in the actual cladding process.

3.3 Element birth and death

The birth and death technology in ANSYS is used to achieve the energy loading of the laser beam. The so-called “death” means that the stiffness matrix of the element is multiplied by an infinitesimal default value to make it infinitely close to 0 when no laser energy is loaded on the corresponding element. Before simulation, all elements built in cladding layers are killed. Therefore, in the laser scanning process, the deactivated element does not participate in the heat transfer process. During the simulation, the elements are activated to participate in the heat conduction process when the laser energy is loaded on the corresponding element.

3.4 Geometric modeling and meshing

Figure 3a shows the finite element model. The size of the cladding layer is 42 mm × 42 mm × 0.6 mm, and the size of the substrate is 60 mm × 60 mm × 6 mm. A gradient mesh is chosen to simplify the model and improve the calculation accuracy; that is, the laser irradiation region and the

Fig. 3 **a** Schematic diagram of finite element geometric model. **b** Schematic diagram of path establishment

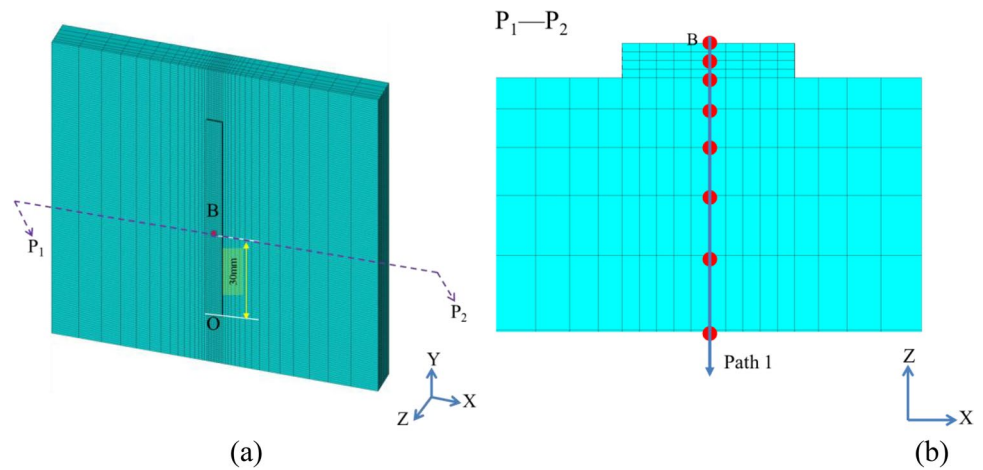


Table 1 Chemical composition of 316L powder wt.%

| Material | C | Si | Mn | P | S | Ni | Cr | Mo |
|----------|------|------|------|-------|------|------|----|-----|
| 316L | 0.03 | 1.00 | 2.00 | 0.035 | 0.03 | 13.5 | 17 | 2.5 |

heat affected zone are more finely divided in the cladding layer, whereas the substrate away from the cladding layer is sparsely divided [21]. The cladding layer grid size is 0.3 mm×0.3 mm×0.1 mm. Node B is located on the upper surface of the cladding layer, and the section P₁-P₂ is the vertical plane of X–Y plane. On the section P₁-P₂, path 1 is along the cladding layer depth, as shown in Fig. 3b.

3.5 Thermo-physical properties of 316L

The substrate material and cladding material are 316L stainless steel. The chemical composition is shown in Table 1.

Combing literature [22] with interpolation method, the thermophysical parameters of the 316L stainless steel material at different temperatures are obtained, as shown in Tables 2 and 3 (ρ -density, T-Celsius, c-specific heat capacity, κ -thermal conductivity, E-elastic modulus, α_t -thermal expansion coefficient, ν -Poisson’s ratio, σ -yield stress, and E' -tangent modulus of the material).

4 Results and discussion

The solid70 element has 8 nodes and 8 temperature degrees of freedom, which can achieve uniform heat flow in three directions, and it is often used in the process of three-dimensional transient thermal analysis. While the solid45 element has 8 nodes and 24 displacement degrees of freedom with large

Table 2 Thermo-physical parameters of 316L stainless steel

| T/(K) | c/(J·kg·K ⁻¹) | κ /(W·m ⁻¹ ·K ⁻¹) | ρ /(kg·m ⁻³) |
|-------|---------------------------|---|-------------------------------|
| 293 | 477 | 13.31 | 7966 |
| 373 | 487 | 14.68 | 7937 |
| 473 | 528 | 16.33 | 7898 |
| 573 | 529 | 17.93 | 7857 |
| 673 | 550 | 19.47 | 7814 |
| 773 | 571 | 20.96 | 7769 |
| 873 | 592 | 22.38 | 7724 |
| 973 | 613 | 23.76 | 7677 |
| 1073 | 634 | 25.07 | 7630 |
| 1173 | 655 | 26.33 | 7583 |
| 1273 | 676 | 27.53 | 7535 |
| 1373 | 698 | 28.67 | 7486 |
| 1473 | 719 | 29.76 | 7436 |
| 1693 | 765 | 31.95 | 7320 |
| 1733 | 765 | 32 | 7320 |

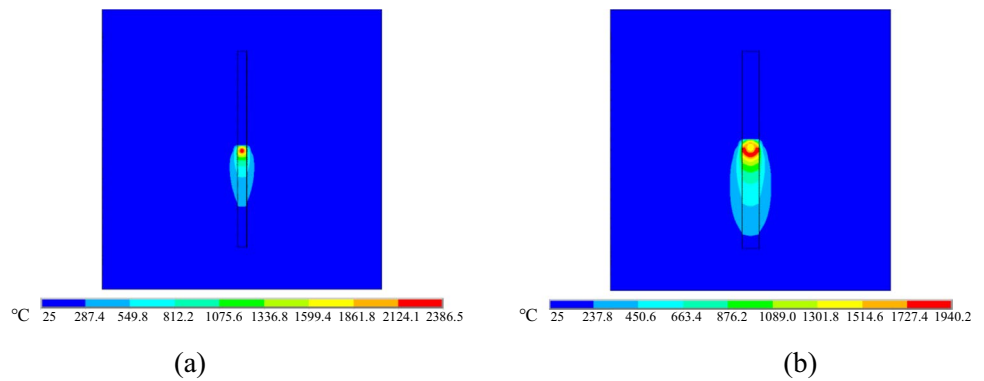
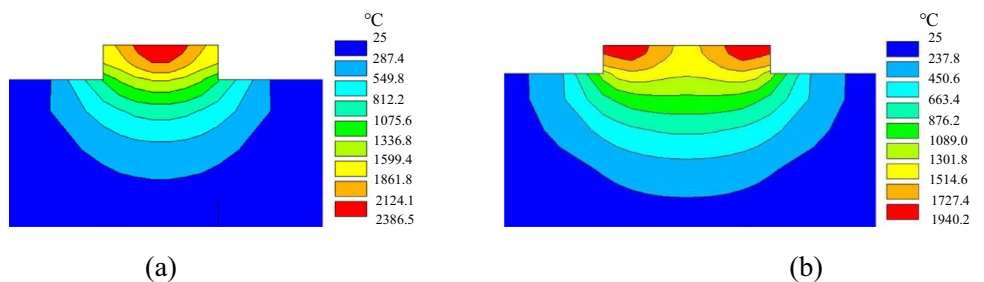
deformation and large strain capacity, it is used as a three-dimensional structural field analysis. So solid70 was adopted as the element type in the temperature field simulation process. The thermal analysis element type solid70 was converted to the structural element type solid45, and all boundary conditions were deleted in the thermal analysis simulation. By loading the temperature data, the results of transient stress, strain, and displacement could be obtained. The numerical simulation process parameters were shown in Table 4.

Table 3 Mechanical properties of 316L stainless steel

| T/(K) | E/(Pa) | $\alpha_t/(K^{-1})$ | ν | $\sigma/(\text{Pa})$ | $E'(\text{Pa})$ |
|-------|----------------------|-----------------------|-------|----------------------|----------------------|
| 293 | $2.21 \cdot 10^{11}$ | $15.24 \cdot 10^{-6}$ | 0.267 | $0.278 \cdot 10^9$ | $2.21 \cdot 10^{10}$ |
| 473 | $1.96 \cdot 10^{11}$ | $16.43 \cdot 10^{-6}$ | 0.290 | $0.193 \cdot 10^9$ | $1.96 \cdot 10^{10}$ |
| 673 | $1.86 \cdot 10^{11}$ | $17.44 \cdot 10^{-6}$ | 0.322 | $0.154 \cdot 10^9$ | $1.86 \cdot 10^{10}$ |
| 873 | $1.71 \cdot 10^{11}$ | $18.21 \cdot 10^{-6}$ | 0.296 | $0.141 \cdot 10^9$ | $1.71 \cdot 10^{10}$ |
| 1073 | $1.32 \cdot 10^{11}$ | $18.83 \cdot 10^{-6}$ | 0.262 | $0.130 \cdot 10^9$ | $1.32 \cdot 10^{10}$ |
| 1173 | $1.17 \cdot 10^{11}$ | $19.11 \cdot 10^{-6}$ | 0.240 | $0.086 \cdot 10^9$ | $1.17 \cdot 10^{10}$ |
| 1273 | $1.01 \cdot 10^{11}$ | $19.38 \cdot 10^{-6}$ | 0.229 | $0.045 \cdot 10^9$ | $1.01 \cdot 10^{10}$ |
| 1373 | $0.81 \cdot 10^{11}$ | $19.66 \cdot 10^{-6}$ | 0.223 | $0.022 \cdot 10^9$ | $0.81 \cdot 10^{10}$ |
| 1473 | $0.35 \cdot 10^{11}$ | $19.95 \cdot 10^{-6}$ | 0.223 | $0.013 \cdot 10^9$ | $0.35 \cdot 10^{10}$ |
| 1693 | $0.02 \cdot 10^{11}$ | $20.7 \cdot 10^{-6}$ | 0.223 | $0.003 \cdot 10^9$ | $0.02 \cdot 10^{10}$ |
| 1733 | $0.02 \cdot 10^{11}$ | $20.7 \cdot 10^{-6}$ | 0.223 | $0.003 \cdot 10^9$ | $0.02 \cdot 10^{10}$ |

Table 4 Laser cladding process parameters

| Power, P(W) | Scanning speed, V(mm/s) | Defocus amount, z (mm) | Laser absorptivity, A | Feeding rate, v (g/min) | Ambient temperature, $T_0(^{\circ}\text{C})$ |
|-------------|-------------------------|------------------------|-----------------------|-------------------------|--|
| 1100 | 6 | 0/−3 | 0.4 | 8 | 25 |

Fig. 4 Temperature distribution with different defocusing amounts: **a** $z=0$ mm and **b** $z=-3$ mm**Fig. 5** The temperature distribution of section P_1 - P_2 with different defocusing amounts: **a** $z=0$ mm and **b** $z=-3$ mm

4.1 Analysis of temperature field results

4.1.1 Temperature distribution

Figure 4 shows the temperature field distribution of the Gaussian laser spot with $z=0$ mm and the hollow-ring

laser spot with $z=-3$ mm at B position, respectively.

According to Fig. 4a, the shape of the spot is circular and solid. The high energy is distributed in the central region of the spot, and temperature reaches 2386.53 °C. While $z=-3$ mm, the spot shape presents “crescent,” and the high energy is distributed in ring region that temperature is up to 1940 °C, as shown in Fig. 4b).

Figure 5 illustrates the temperature distribution of P_1 - P_2 section when the spot center is located at B position.

It can be seen from Fig. 5a that the high temperature region concentrates in the middle of the cladding layer, and the temperature on both sides is relatively low. On the contrary, high temperature region is concentrated on both sides of the cladding layer, and the temperature in the middle region is lower, as shown in Fig. 5b.

4.1.2 Characteristics of temperature curve

Figure 6a shows the temperature change curve of node B with time under different defocusing amounts.

According to Fig. 6, node B experiences one temperature peak during the cladding process, and the temperature

changes relatively drastic when $z=0$ mm, which reflected that the laser cladding is a transient process of rapid heat and cooling. While $z=-3$ mm, node B experiences two temperature peak, and the latter temperature peak is higher than the previous one during the cladding process, which is related to the energy distribution of the hollow laser.

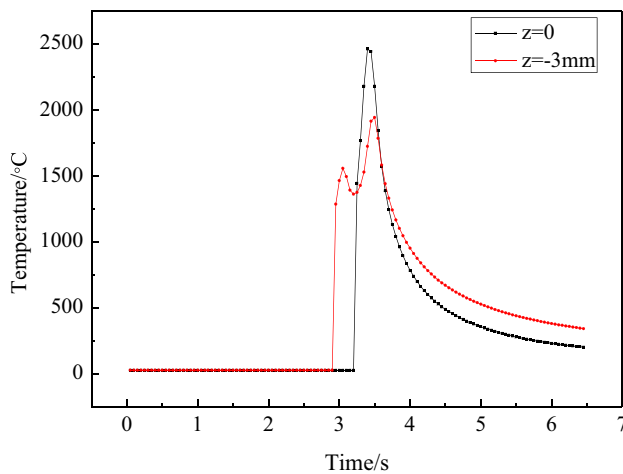


Fig. 6 Temperature change curve of node B under different defocusing amounts

By comparing the temperature change curves of the two energy distributions, the temperature change is relatively gentle when $z = -3$ mm, which is conducive to reduce the temperature gradient.

4.1.3 Characteristics of temperature gradient

The temperature gradient distributions on path 1 under different defocusing amounts are illustrated in Fig. 7.

As shown in Fig. 7, the temperature gradient distribution on path 1 first increases and then decreases. That is, the temperature gradient is large in the cladding layer and reaches the maximum at the joint surface between the cladding layer and the substrate and then drops rapidly as it goes deep into the substrate region.

The maximum temperature gradient reaches 1.78×10^6 °C/m when $z = 0$ mm. While $z = -3$ mm, the maximum temperature gradient is only 4.95×10^5 °C/m, which is 72.3% lower than that $z = 0$ mm. Thus, the temperature gradient of the cladding layer can be significantly reduced when $z = -3$ mm, which is beneficial to reduce the internal stress of the cladding layer.

4.2 Analysis of stress field results

4.2.1 Residual stress distribution

Figure 8 shows the residual stress distributions in X, Y, Z directions and Von-Mises when $z = -3$ mm. The X direction residual stress distribution is symmetrical at both ends of the joint surface, and maximum residual stress value reaches 236 MPa, whereas the cladding layer presents low

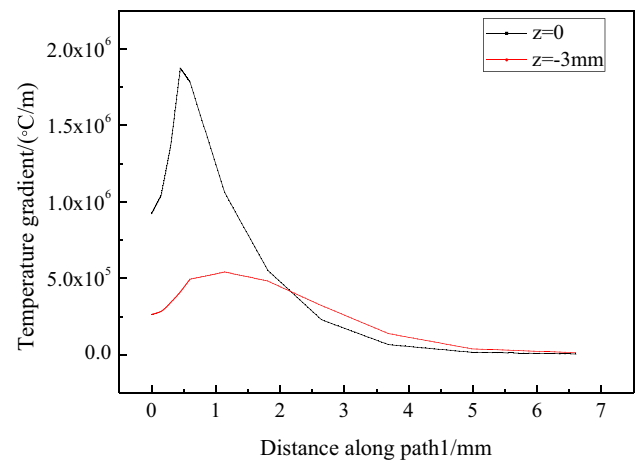


Fig. 7 Temperature gradient distribution on path 1 under different defocusing amounts

stress state. The residual stress in Y direction of the cladding layer is tensile stress, and the high residual stress is distributed on the upper surface of the cladding layer, and the maximum value reaches 273 MPa; the region away from the cladding layer is compressive stress. The overall residual stress in Z direction is low, and the cladding layer presents compressive stress. The equivalent stress distribution presents “dumbbell” shape, the maximum stress is distributed at the beginning of the cladding, and the maximum value reaches 299 MPa.

The above analysis showed that the residual stress in Y direction was the largest and the main stress. Therefore, the residual stress in Y direction is mainly studied in this paper.

4.2.2 Stress distribution on the path

Figure 9 illustrates the Y direction residual stress distribution on cladding layer along path 1 under different defocusing amounts.

According to Fig. 9, the Y direction residual stress distribution tendency of cladding layer on path 1 is consistent under different defocusing amounts. The residual stress first increases and then decreases with the increase of the cladding layer depth and reaches maximum value at 1/4 position from the joint surface. The comparison shows that the residual stress is larger when $z = 0$ mm than $z = -3$ mm. This can be interpreted as the concentration of laser energy at the focal point, and the cladding layer absorbs more energy when $z = 0$ mm, resulting in large temperature gradient.

Therefore, the residual stress of cladding layer can be reduced when $z = -3$ mm, which is conducive to reduce crack tendency, and it proves the superiority of hollow laser cladding process and the rationality of energy distribution.

Fig. 8 Residual stress distribution in different directions: **a** X direction stress, **b** Y direction stress, **c** Z direction stress, and **d** equivalent stress

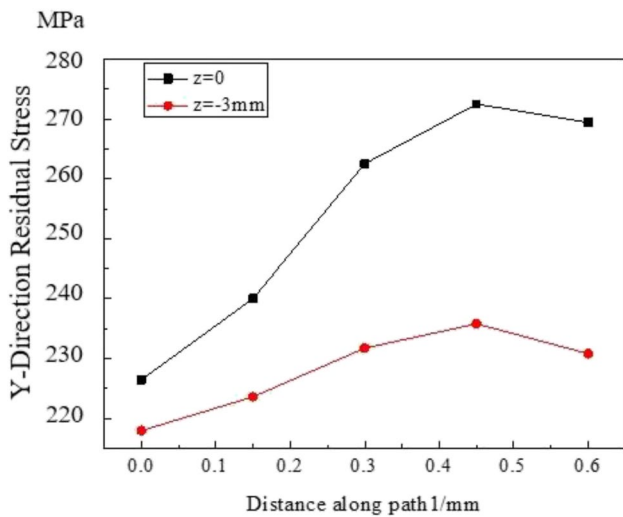
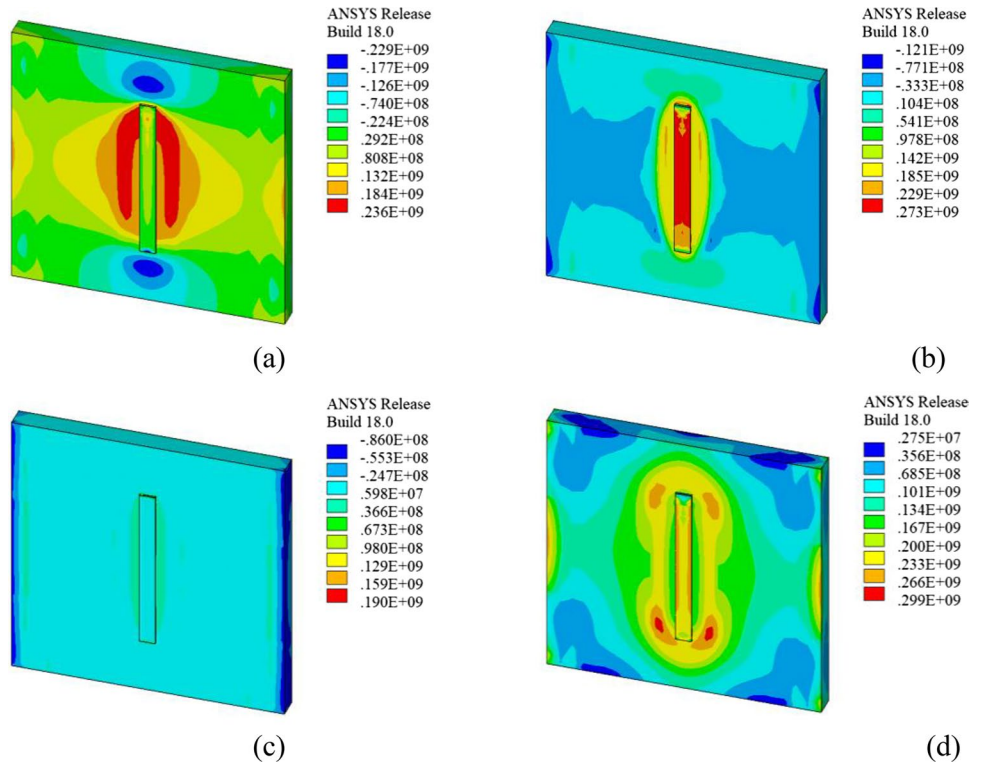


Fig. 9 Y direction stress distribution on path 1 under different defocusing amounts

5 Experiment procedure

Figure 10 shows the experimental setup applied for the laser cladding process. The system includes IPG YLS-2000-TR high-power fiber laser, GTV PF2/2 M powder feeder, 6-axis KUKA robot, powder feeding system, tilting rotary table, and gas system.

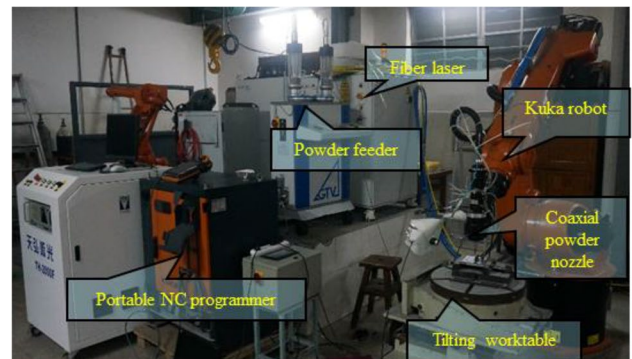


Fig. 10 Schematic diagram of the experimental setup

5.1 Experimental results and analysis

5.1.1 Laser energy distribution test

This paper adopted beam monitor laser analysis meter to measure the energy density distribution of hollow laser spot, and the test results are shown in Fig. 11.

According to the test data from Fig. 11a, the energy of the hollow laser at the focal point ($z=0$) presents a Gaussian distribution. But the energy shows two Gaussian-like energy distribution on both sides of the center line, and there is no energy distribution near the center line when $z=-3$ mm, as

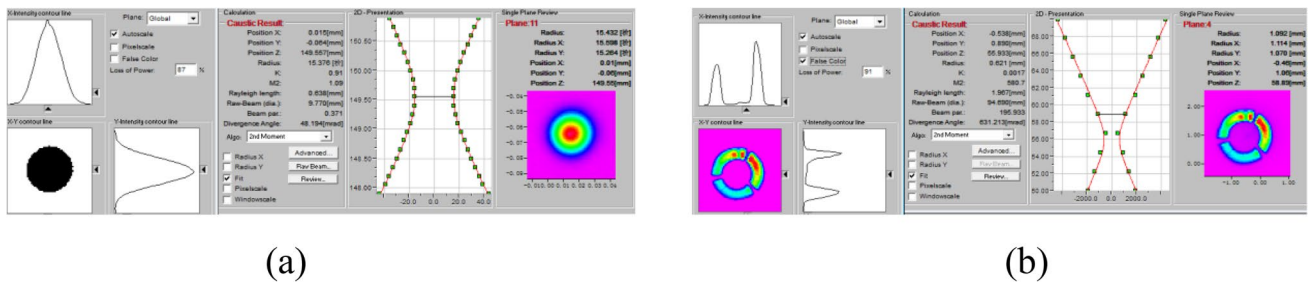
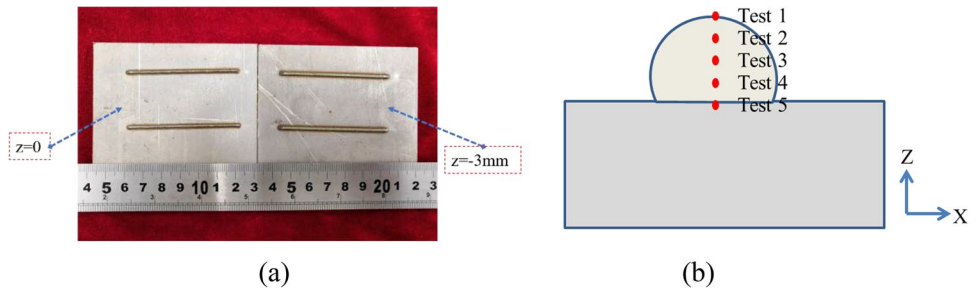


Fig. 11 Energy density distribution with different defocusing amount: a $z=0$ and b $z=-3$ mm

Fig. 12 a Single-track laser cladding samples with different defocusing amounts and b schematic diagram of residual stress test point on cladding layer



shown in Fig. 11b, which is consistent with the temperature field analysis results.

5.1.2 Residual stress test results

In this paper, single-track laser cladding experiments were carried out with process parameters which were consistent with numerical simulation, and the samples are shown in Fig. 12a. The X-350A stress tester was adopted to measure the residual stress of the sample. In order to obtain the residual stress in depth of cladding layer, the surface of cladding layer was stripped and polished electrolytically using saturated NH_4Cl -solution. The measurement points were five along depth direction of the cladding layer as shown in Fig. 12b.

The residual stress test results in Y direction are shown in Fig. 13.

According to Fig. 13, the residual stress measured in the experiment showed a tendency which was firstly increasing and then decreasing with the depth growth. The overall stress presented tensile stress, and the maximum residual stress appeared at 1/4 position away from the joint surface, which was consistent with the simulation and verified the correctness of the numerical simulation. Meanwhile, some differences existed between numerical simulation and experiment results. The main reasons were as follows: on the one hand, the model assumption was simplified, and the finite element mesh could not be meshed thinly, which led to calculation deviation. On the other hand, part

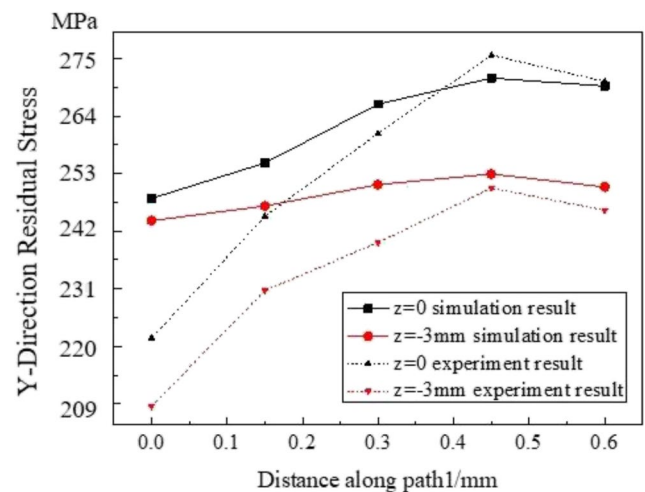


Fig. 13 Comparison of experimental results and simulation results

of residual stress would be released during the stripping process in the experiment, which affected the accuracy of the measurement.

5.1.3 Microstructure analysis

The microstructure of the component determines the mechanical properties and performance. The optical examination was carried out on samples with defocusing amount of $z=0$ and $z=-3$ mm. The microstructure was examined in the adjacent region of the top, middle, and bottom, respectively, as shown in Fig. 14.

As can be seen from Fig. 14, no pores and microcracks were observed in the cross section. It can be identified that the microstructure shows a mixture of dendrite and cellular structures. The difference is that the finest microstructure is shown on the top. The microstructure at the bottom is dendrite structures, because the deposited layers at the bottom are close to the substrate, and the temperature gradient is more than the middle and top. Therefore, it is suggested that the difference of the microstructure resulted from the different molten pool temperature gradients. Comparing with the Gaussian laser, the microstructure was finer and more uniform using hollow-ring laser.

6 Discussion

According to formula 1, the energy distribution of the hollow-ring laser can be changed by adjusting the laser defocusing amount. The schematic diagram of different energy distributions are shown in Fig. 15 with increase of laser defocusing amount along scanning direction.

In the Gaussian heat source mode, the energy along the scanning direction is more concentrated in the center zone, and the energy of the edge zone is low, and the energy distribution is not helping to form flat cladding layer, especially the cladding layer in the edge that is easy to appear inadequate melting phenomenon, reducing the surface accuracy and forming the quality of the formed parts. In the hollowing heat source mode, the solid light spot becomes a ring spot; that is, the energy concentration zone changes from the center to the outer edge. The laser energy distribution presents a “saddle” shape, and the energy distribution is more uniform and reasonable, which can eliminate the inadequate phenomenon of the cladding edge. It can improve the poor metallurgical bonding under Gaussian light source. At the same time, comparing with the Gaussian laser, temperature

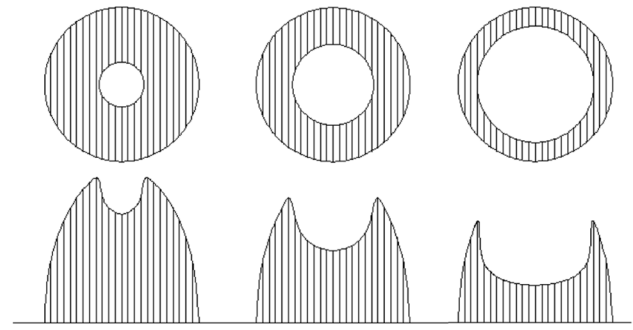


Fig. 15 Energy distribution of hollow-ring laser with increase of laser defocusing amount along scanning direction

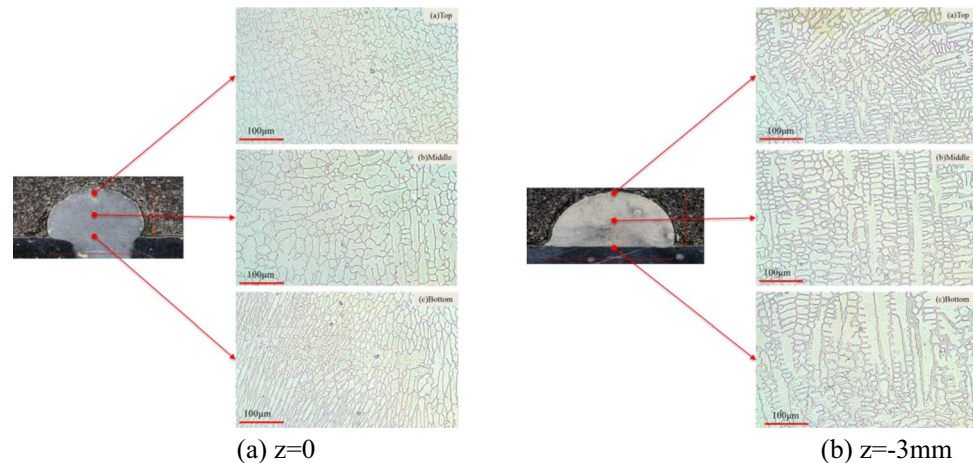
peaks and temperature changed relatively gentle, and the maximum residual stress decreased when used the hollow-ring laser.

7 Conclusion

In order to discuss the influence of the Gaussian and hollow-ring laser modes on temperature and stress fields in cladding layers, a 3D finite element method is established, and experimental verification is performed with the same process parameters. The conclusions are as follows.

- (1) The temperature of node on the cladding changed sharply, and the temperature gradient was large when $z=0$ mm, while the temperature distribution was more uniform, and the temperature gradient was smaller when $z=-3$ mm.
- (2) The residual stress in Y direction of the cladding layer was the largest, and the residual stress was higher when $z=0$ mm. Residual stress level could be effectively reduced when $z=-3$ mm, which was beneficial to reduce the cracking tendency of cladding.

Fig. 14 Microstructure of samples with different defocusing amounts at different positions



- (3) Through the microstructure analysis and comparison, the grain size difference between the top, middle, and bottom of the cladding was smaller than $z=0$ mm, which proved the uniformity and rationality when $z=-3$ mm.

Funding The work was financially supported by the Sci-Tech Plan Project of Suzhou municipal of China through grant no. SYC2022143 and the National Key Research Program of China through grant no.2016YFB1100300.

Declarations

Ethics approval Not applicable.

Consent to participate Not applicable.

Consent for publication Not applicable.

Conflict of interest The authors declare no competing interests.

References

- Weng F, Chen CZ, Yu HJ (2014) Research status of laser cladding on titanium and its alloys: a review. *Mater Design* 58:412–425
- Zeng C, Tian W, Liao WH, Hua L (2016) Microstructure and porosity evaluation in laser-cladding deposited Ni-based coatings. *Surf Coat Technol* 294:122–30
- Yang J, Chen J, Yang HO, Lin X, Huang WD (2004) Experimental study on residual stress distribution of laser rapid forming process. *Rare Met Mater Eng* 33(12):1304–1307
- Tseng WC, Aoh JN (2013) Simulation study on laser cladding on preplaced powder layer with a tailored laser heat source. *Opt Laser Technol* 48:141–152
- Sun ST, Fu HG, Chen SY, Ping XL, Wang KM, Guo XY, Lin J, Lei YP (2019) A numerical-experimental investigation of heat distribution, stress field and crack susceptibility in Ni60A coatings. *Opt Laser Technol* 117:175–185
- Wang H (2014) Effect of process parameters on residual stress distribution during direct laser metal deposition. *Adv Mater Res* 989(994):49–54
- Heigel JC, Michaleris P, Reutzel EW (2015) Thermo-mechanical model development and validation of directed energy deposition additive manufacturing of Ti-6Al-4V. *Addit Manuf* 5:9–19
- Yan ZR, Liu WW, Tang ZJ, Liu XY (2019) Effect of thermal characteristics on distortion in laser cladding of AISI 316L. *J Manuf Process* 44:309–318
- Krzyzanowski M, Bajda S, Liu YJ, Triantaphyllou A, Rainforth WM, Glendenning M (2016) 3D analysis of thermal and stress evolution during laser cladding of bioactive glass coatings. *J Mech Behav Biomed Mater* 59:404–417
- Wang T, Qin LC, Liu JQ (2019) Parameter analysis of thermal behavior during laser melting of Ti-6Al-4V alloy powder. *Int J Adv Manuf Technol* 104(5–8):2875–2885
- Liu HM, Qin XP, Wu MW (2019) Numerical simulation of thermal and stress field of single track cladding in wide-beam laser cladding. *Int J Adv Manuf Technol* 104(9–12):3959–3976
- Shi SH, Fu GY, Wang AJ, Zhang Y, Zhu PF, Hu J (2006) Internal powder feeding technology and nozzle through a hollow laser beam in laser processing forming manufacturing. *Chinses Patent CN200610116413,2006-09-22*
- Shi GL, Shi SH, Wu SH (2010) Research on effective utilization rate of power in inside-laser coaxial powder feeding laser cladding and rapid prototyping process. *Hot Working Technol* 7:152–161
- Shi JJ (2019) Mechanism study of non-supportive overhang part by hollow laser cladding forming. *Soochow University, Su zhou*
- Liu Y, Zhang J, Pang ZC (2018) Numerical and experimental investigation into the subsequent thermal cycling during selective laser melting of multi-layer 316 L stainless steel. *Opt Laser Technol* 98:23–32
- Hussein A, Hao L, Yan C, Everson R (2013) Finite element simulation of temperature and stress in single layers built without-support in selective laser melting. *Mate Des* 52:638–647
- Mohammadpour M, Yazdian N, Yang G, Wang HP, Carlson B, Kovacevic R (2018) Effect of dual laser beam on dissimilar welding-brazing of aluminum to galvanized steel. *Opt Laser Technol* 98:214–228
- Santhanakrishnan S, Kong F, Kovacevic R (2011) An experimentally based thermo-kinetic hardening model for high power direct diode laser cladding. *J Mater Process Technol* 211(7):1247–1259
- Capello E, Castrelnovo M, Previtali B, Vedali M (2007) Surface treatment of welded duplex stainless steels by diode laser. *J Laser Appl* 19(3):133–140
- Farahmand P, Kovacevic R (2014) An experimental–numerical investigation of heat distribution and stress field in single-and multi-track laser cladding by a high-power direct diode laser. *Opt Laser Technol* 63:154–168
- Gao WY, Zhao SS, Wang YB, Liu FL, Zhou CY, Lin XC (2014) Effect of re-melting on the cladding coating of Fe-based composite powder. *Mater Des* 64(9):490–496
- Jiang W, Yahiaoui K, Hall FR (2005) Finite element predictions of temperature distributions in a multi pass welded piping branch junction. *J Pressure Vessel* 127(1):7–12

Publisher's note Springer Nature remains neutral with regard to jurisdictional claims in published maps and institutional affiliations.

Springer Nature or its licensor (e.g. a society or other partner) holds exclusive rights to this article under a publishing agreement with the author(s) or other rightsholder(s); author self-archiving of the accepted manuscript version of this article is solely governed by the terms of such publishing agreement and applicable law.